

Supporting Information for

**Brønsted Acid Strength Does Not Change for Bulk and External Sites of MFI Except Al Substituted Where Silanol Groups Form**

Haliey Balcom<sup>a†</sup>, Alexander J. Hoffman<sup>a§†</sup>, Huston Loch<sup>a#</sup>, David Hibbitts<sup>a\*</sup>

*<sup>a</sup>Department of Chemical Engineering, University of Florida, Gainesville, FL 32611*

\*corresponding author, email: [hibbitts@che.ufl.edu](mailto:hibbitts@che.ufl.edu)

Present addresses

§A.H.: Massachusetts Institute of Technology, Cambridge, MA 02139, USA

#H.L.: University of Illinois at Urbana-Champaign, Urbana, IL 61801, USA

†These authors contributed equally

## Table of Contents

Section S1. Structures of H-form and NH <sub>4</sub> -form bulk MFI model .....	S4
Section S2. Electron affinities in bulk MFI model .....	S10
Section S3. Relationship between NH <sub>3</sub> binding energy and DHE .....	S11
Section S4. Structures of H-form and NH <sub>4</sub> -form surface MFI model .....	S12
Section S5. DPE dependence on vacuum space in surface model .....	S28
Section S6. Derivation of rate ratio equation for external and internal sites .....	S31
References .....	S34

## List of Tables and Figures

Figure S1 .....	S4
Figure S2 .....	S5
Figure S3 .....	S6
Figure S4 .....	S7
Figure S5 .....	S8
Figure S6 .....	S9
Table S1 .....	S10
Figure S7 .....	S11
Figure S8 .....	S12
Figure S9 .....	S13
Figure S10 .....	S14
Figure S11 .....	S15
Figure S12 .....	S16
Figure S13 .....	S17
Figure S14 .....	S18
Figure S15 .....	S19
Figure S16 .....	S20
Figure S17 .....	S21
Figure S18 .....	S22
Figure S19 .....	S23

Figure S20.....	S24
Figure S21.....	S25
Figure S22.....	S26
Figure S23.....	S27
Figure S24.....	S28
Figure S25.....	S29
Figure S26.....	S30
Figure S27.....	S33

# **S1. Structures of H-form and NH<sub>4</sub>-form bulk MFI model**

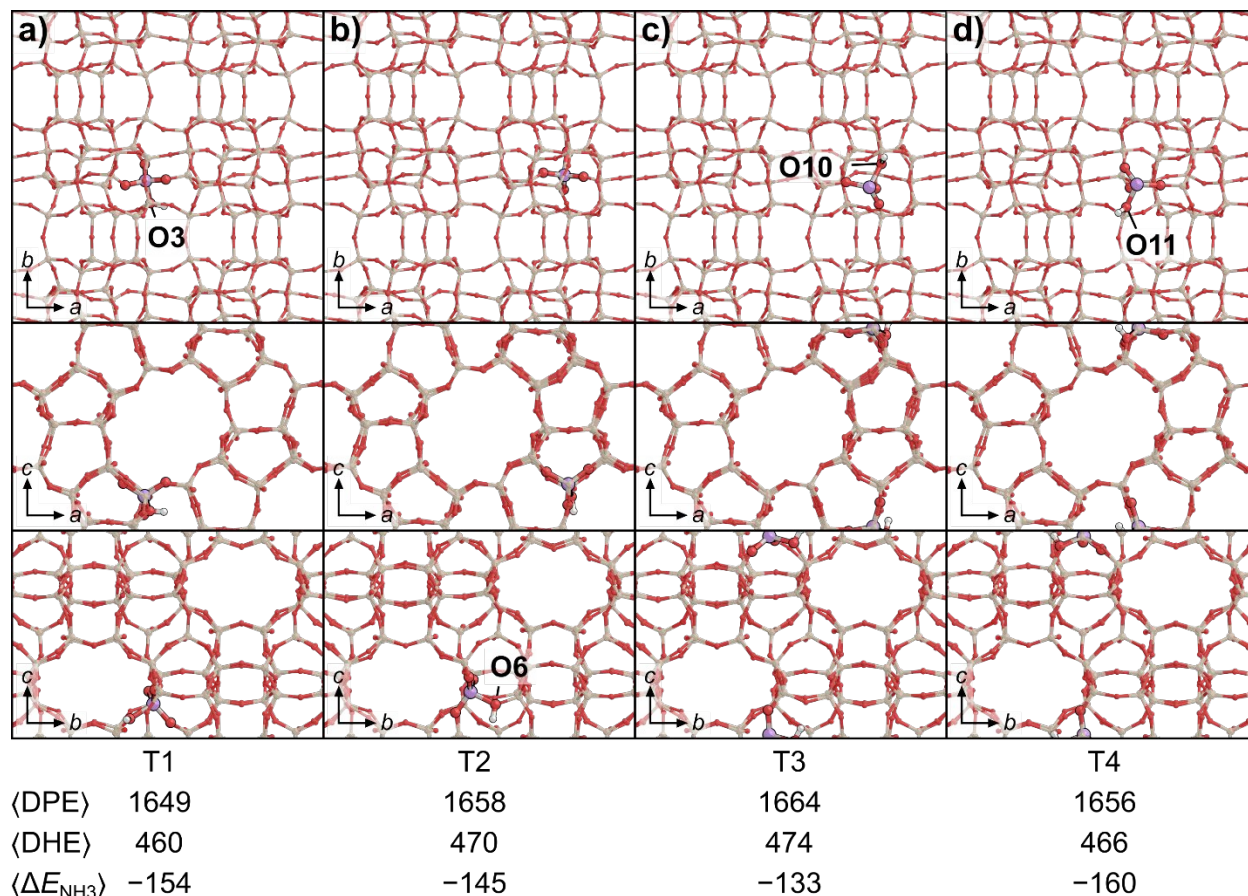


**Figure S1.** Structures of the most stable H-form with a proton at (a) O3 on T1, (b) O6 on T2, (c) O10 on T3, and (d) O11 on T4. Structures are shown down the *c*-vector (top), down the *b*-vector and straight channel (middle), and down the *a*-vector and sinusoidal channel (bottom). The ensemble average DPE, DHE, and  $\Delta E_{\text{NH}_3}$  are shown for each T-site beneath the corresponding structure, all in kJ mol<sup>-1</sup>.



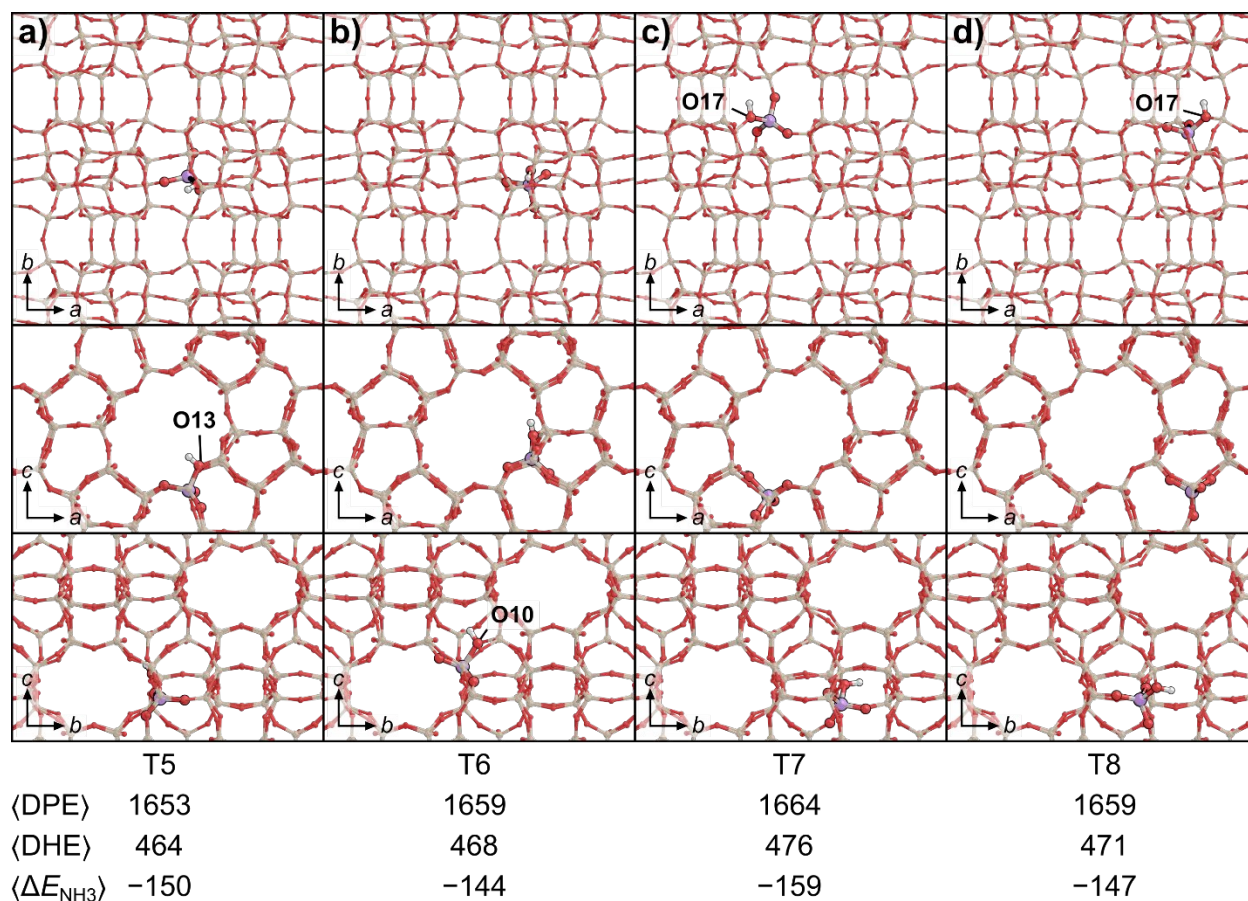


**Figure S2.** Structures of the most stable H-form with a proton at (a) O13 on T5, (b) O10 on T6, (c) O17 on T7, and (d) O17 on T8. Structures are shown down the  $c$ -vector (top), down the  $b$ -vector and straight channel (middle), and down the  $a$ -vector and sinusoidal channel (bottom). The ensemble average DPE, DHE, and  $\Delta E_{\text{NH}_3}$  are shown for each T-site beneath the corresponding structure, all in  $\text{kJ mol}^{-1}$ .

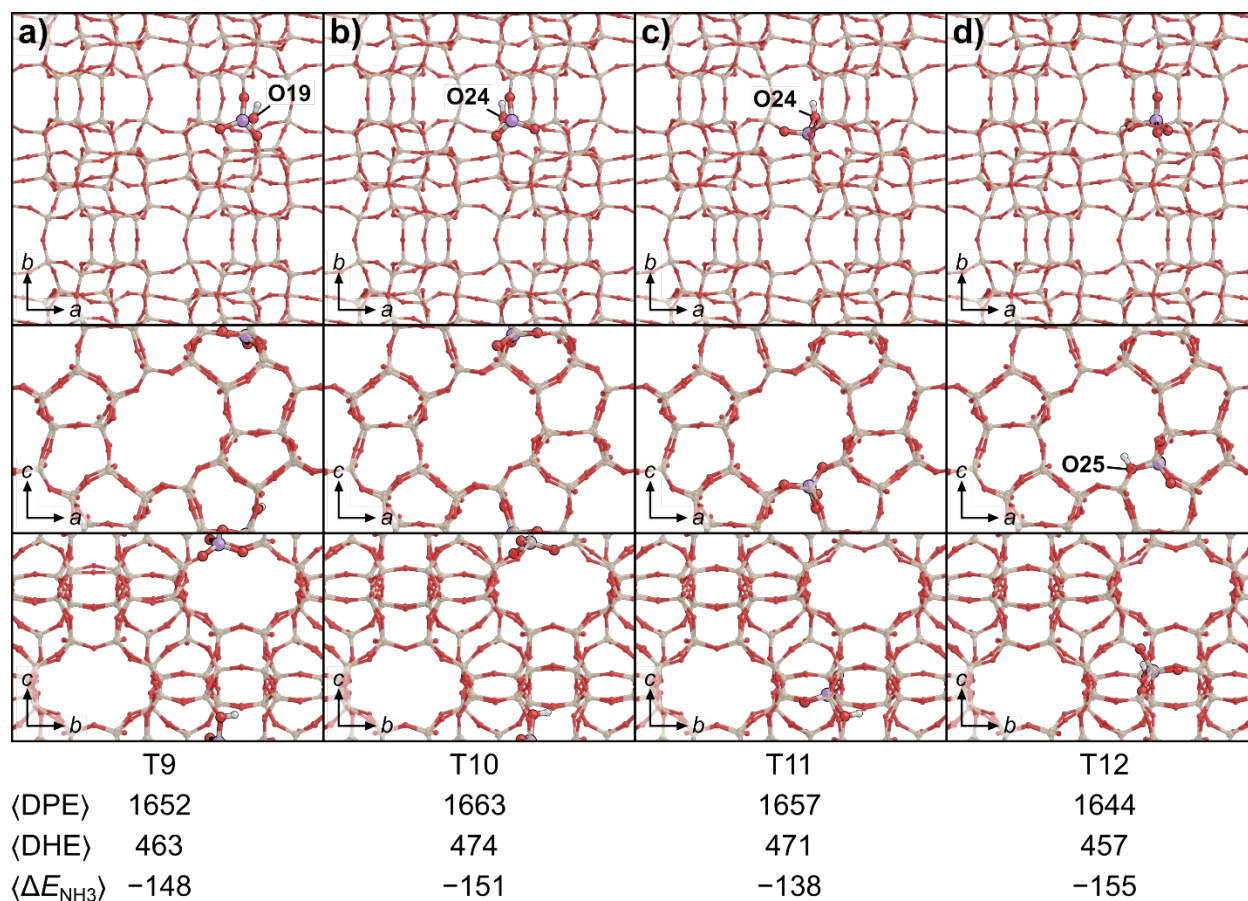


**Figure S3.** Structures of the most stable H-form with a proton at (a) O19 on T9, (b) O24 on T10, (c) O24 on T11, and (d) O25 on T12. Structures are shown down the  $c$ -vector (top), down the  $b$ -vector and straight channel (middle), and down the  $a$ -vector and sinusoidal channel (bottom). The ensemble average DPE, DHE, and  $\Delta E_{\text{NH}_3}$  are shown for each T-site beneath the corresponding structure, all in  $\text{kJ mol}^{-1}$ .

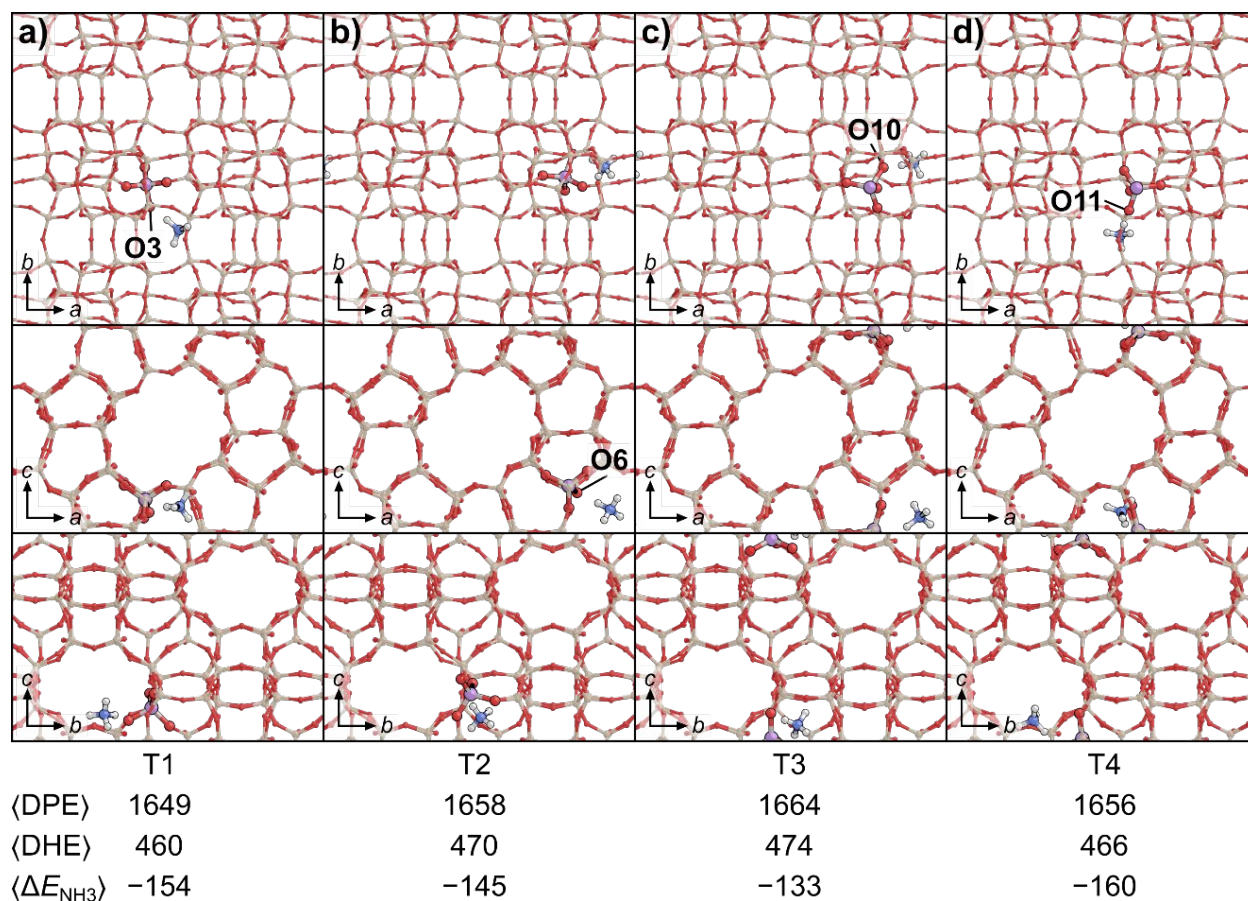


**Figure S4.** Structures of the most stable  $\text{NH}_4$ -form with the  $\text{NH}_4^+$  at (a) O3 on T1, (b) O6 on T2, (c) O10 on T3, and (d) O11 on T4. Structures are shown down the  $c$ -vector (top), down the  $b$ -vector and straight channel (middle), and down the  $a$ -vector and sinusoidal channel (bottom). The ensemble average DPE, DHE, and  $\Delta E_{\text{NH}_3}$  are shown for each T-site beneath the corresponding structure, all in  $\text{kJ mol}^{-1}$ .

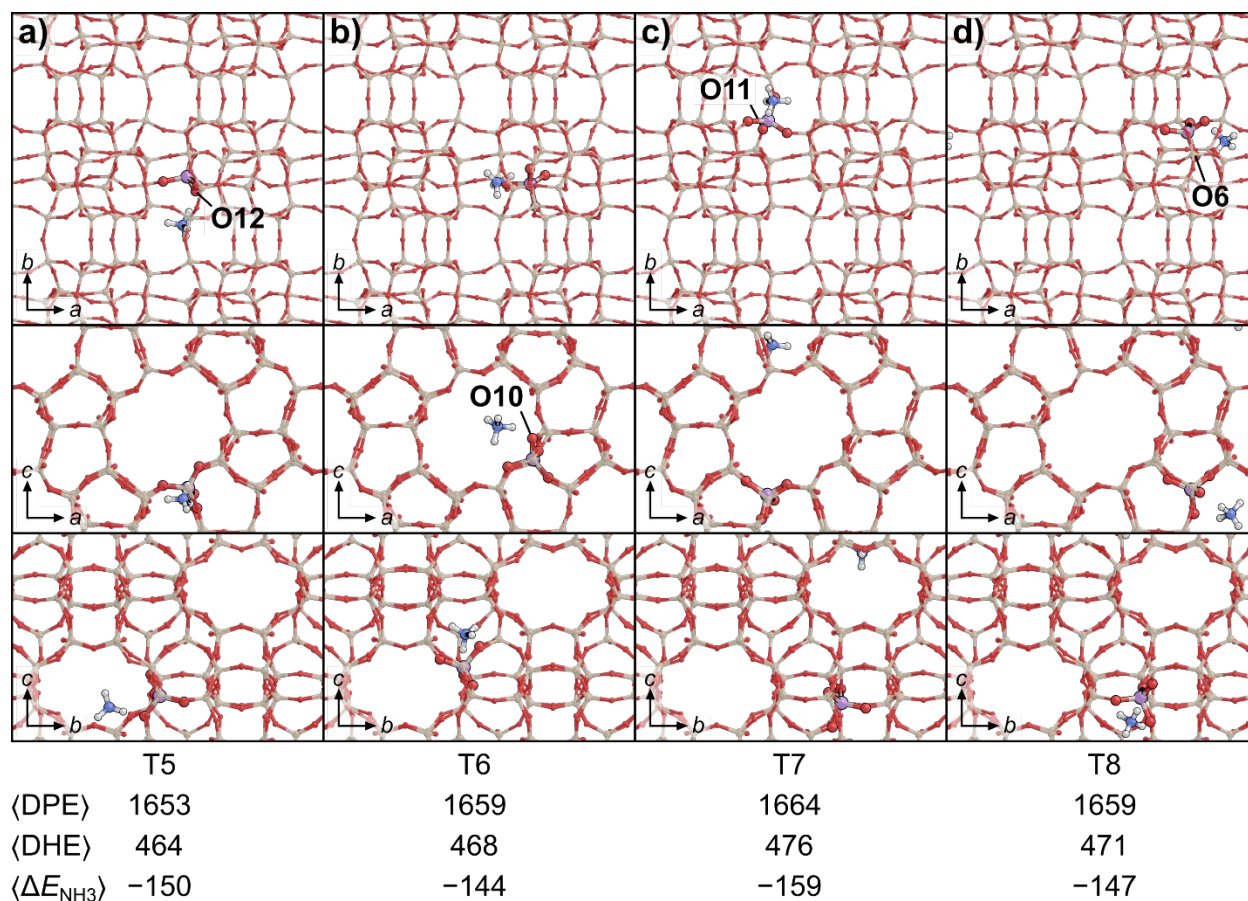


**Figure S5.** Structures of the most stable  $\text{NH}_4$ -form with the  $\text{NH}_4^+$  at (a) O12 on T5, (b) O10 on T6, (c) O11 on T7, and (d) O6 on T8. Structures are shown down the  $c$ -vector (top), down the  $b$ -vector and straight channel (middle), and down the  $a$ -vector and sinusoidal channel (bottom). The ensemble average DPE, DHE, and  $\Delta E_{\text{NH}_3}$  are shown for each T-site beneath the corresponding structure, all in  $\text{kJ mol}^{-1}$ .



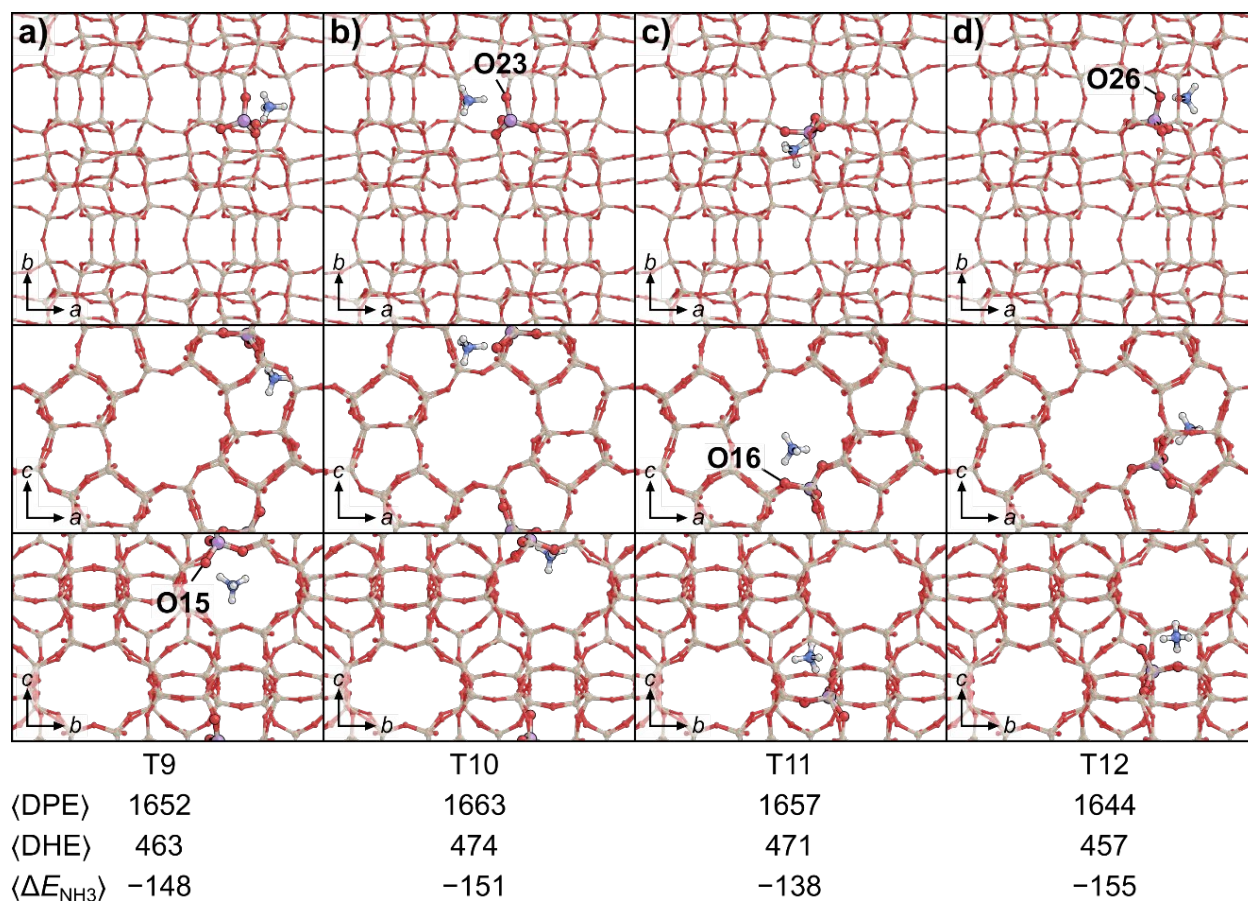


**Figure S6.** Structures of the most stable  $\text{NH}_4$ -form with the  $\text{NH}_4^+$  at (a) O15 on T9, (b) O23 on T10, (c) O16 on T11, and (d) O26 on T12. Structures are shown down the  $c$ -vector (top), down the  $b$ -vector and straight channel (middle), and down the  $a$ -vector and sinusoidal channel (bottom). The ensemble average DPE, DHE, and  $\Delta E_{\text{NH}_3}$  are shown for each T-site beneath the corresponding structure, all in  $\text{kJ mol}^{-1}$ .

## S2. Electron affinities in bulk MFI model

**Table S1.** Electron affinities (EA) for each T-site in the bulk MFI in kJ mol<sup>-1</sup>.

T-site	EA / kJ mol <sup>-1</sup>
T1	-121
T2	-122
T3	-120
T4	-120
T5	-121
T6	-120
T7	-122
T8	-122
T9	-121
T10	-122
T11	-124
T12	-124

### S3. Relationship between $\text{NH}_3$ binding energy and DHE

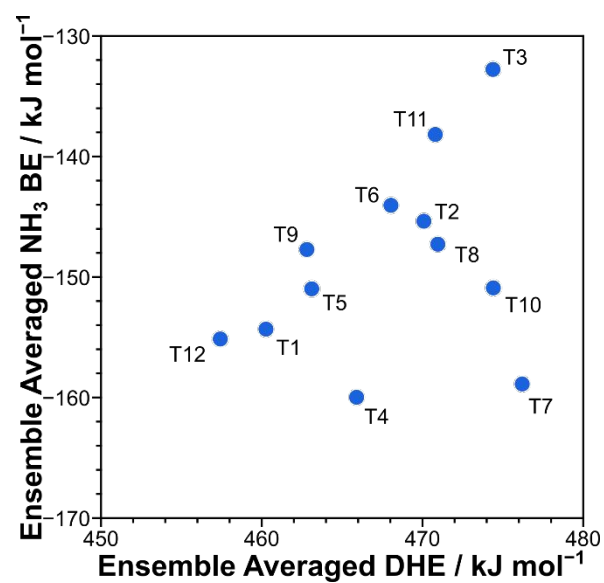


**Figure S7.** Relationship between ensemble averaged  $\text{NH}_3$  binding energy ( $\text{NH}_3$  BE) and ensemble averaged DHE, both in  $\text{kJ mol}^{-1}$ , in bulk MFI.

#### S4. Structures of H-form and NH<sub>4</sub>-form surface MFI model

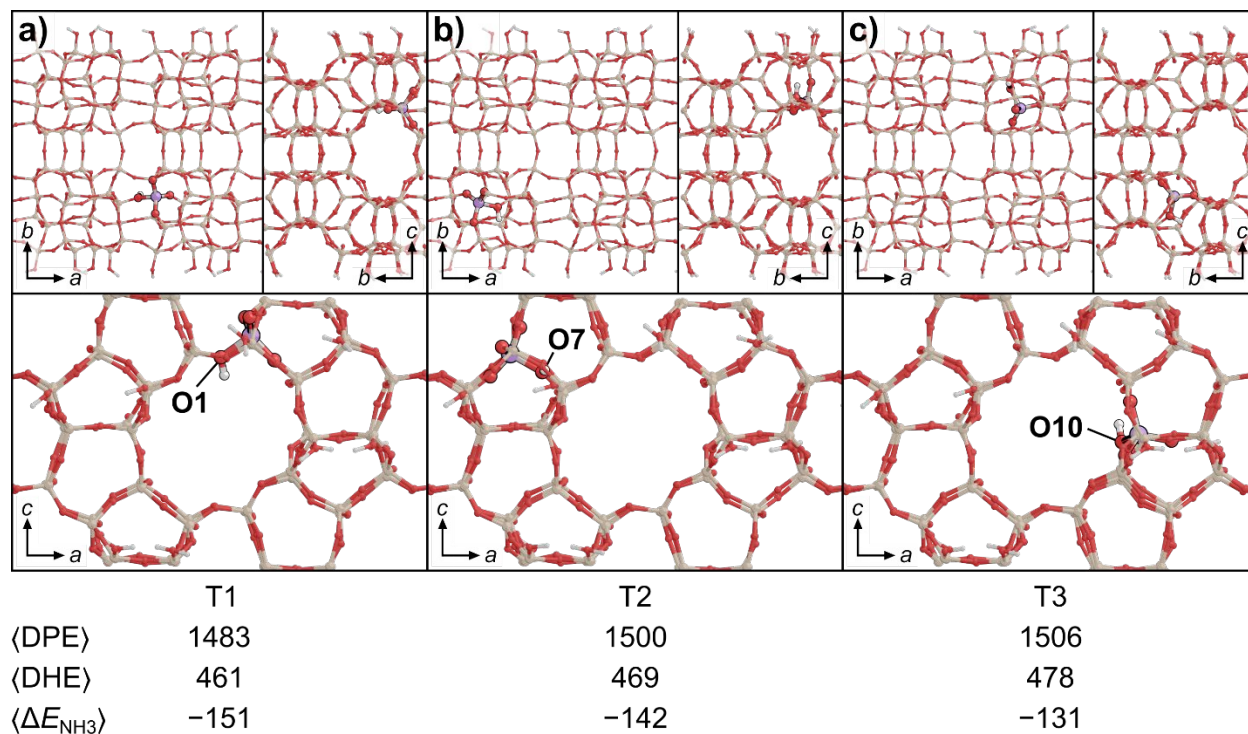


**Figure S8.** Structures of the most stable H-form on the surface model for internal Al positions with the proton at (a) O1 on T1, (b) O7 on T2, and (c) O10 on T3. Structures are shown down the  $c$ -vector (top left), down the  $a$ -vector and sinusoidal channel (top right), and down the  $b$ -vector and straight channel (bottom). The ensemble average DPE (extrapolated to 0 Å of vacuum space, see Section 3.2 of the main text), DHE, and  $\Delta E_{\text{NH}_3}$  are shown for each T-site beneath the corresponding structure, all in kJ mol<sup>-1</sup>.



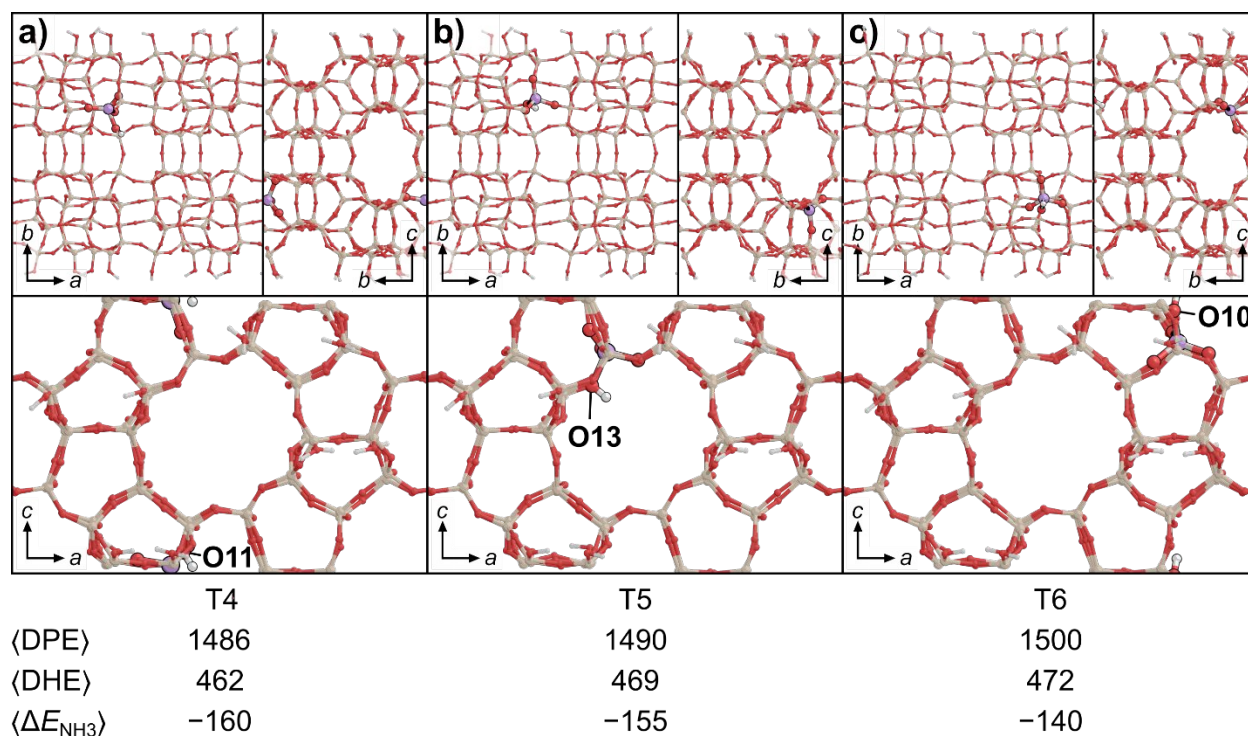


**Figure S9.** Structures of the most stable H-form on the surface model for internal Al positions with the proton at (a) O11 on T4, (b) O13 on T5, and (c) O10 on T6. Structures are shown down the  $c$ -vector (top left), down the  $a$ -vector and sinusoidal channel (top right), and down the  $b$ -vector and straight channel (bottom). The ensemble average DPE (extrapolated to 0 Å of vacuum space, see Section 3.2 of the main text), DHE, and  $\Delta E_{\text{NH}_3}$  are shown for each T-site beneath the corresponding structure, all in  $\text{kJ mol}^{-1}$ .

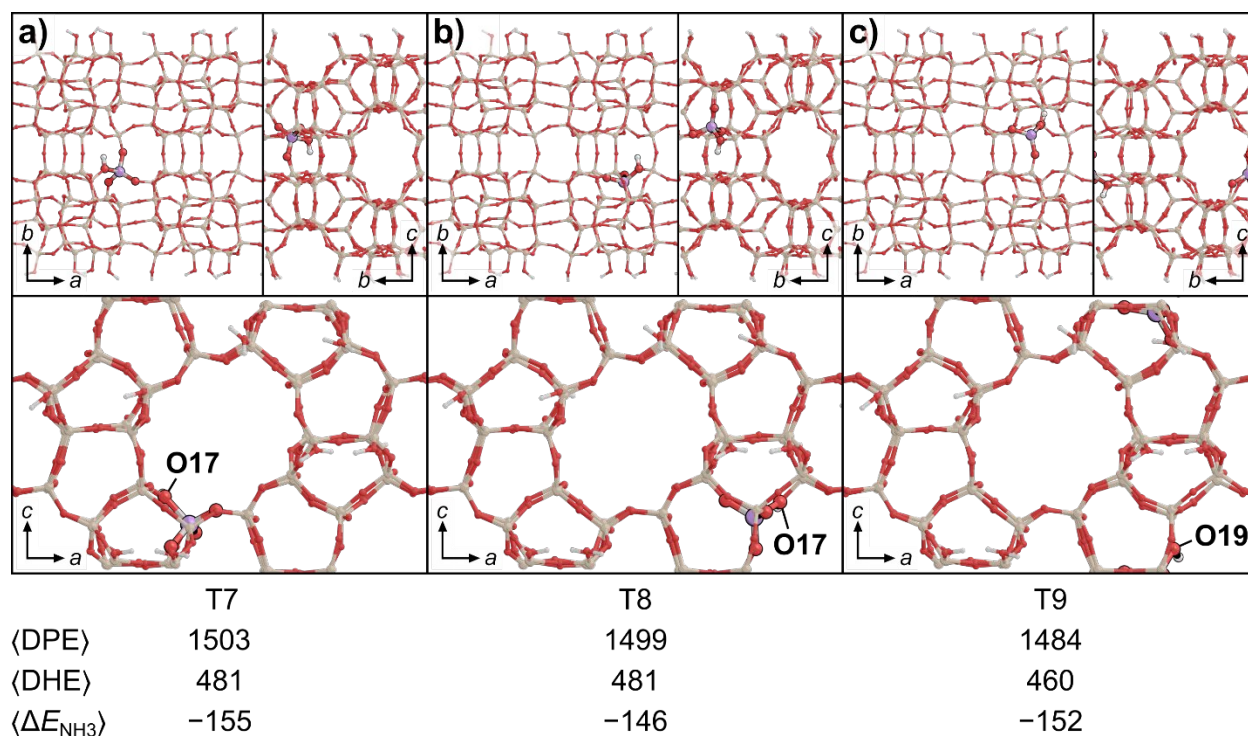


**Figure S10.** Structures of the most stable H-form on the surface model for internal Al positions with the proton at (a) O17 on T7, (b) O17 on T8, and (c) O19 on T9. Structures are shown down the  $c$ -vector (top left), down the  $a$ -vector and sinusoidal channel (top right), and down the  $b$ -vector and straight channel (bottom). The ensemble average DPE (extrapolated to 0 Å of vacuum space, see Section 3.2 of the main text), DHE, and  $\Delta E_{\text{NH}_3}$  are shown for each T-site beneath the corresponding structure, all in  $\text{kJ mol}^{-1}$ .

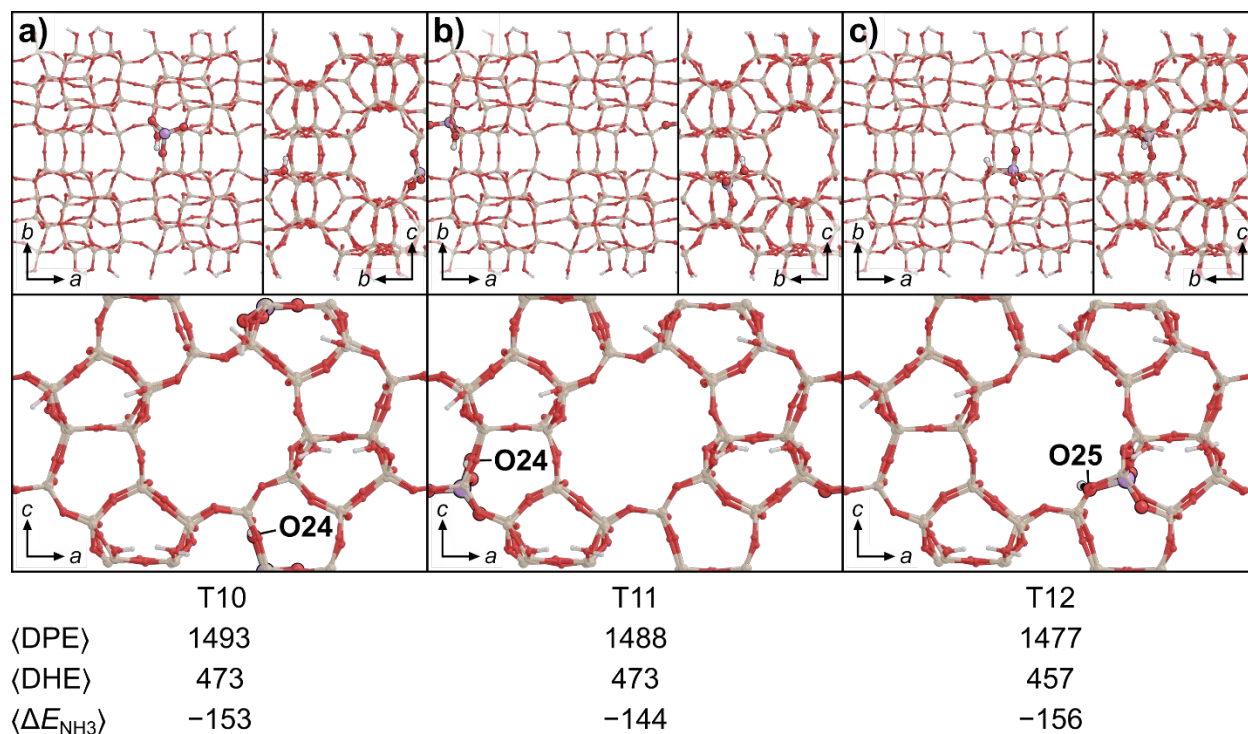


**Figure S11.** Structures of the most stable H-form on the surface model for internal Al positions with the proton at (a) O24 on T10, (b) O24 on T11, and (c) O25 on T12. Structures are shown down the  $c$ -vector (top left), down the  $a$ -vector and sinusoidal channel (top right), and down the  $b$ -vector and straight channel (bottom). The ensemble average DPE (extrapolated to 0 Å of vacuum space, see Section 3.2 of the main text), DHE, and  $\Delta E_{\text{NH}_3}$  are shown for each T-site beneath the corresponding structure, all in  $\text{kJ mol}^{-1}$ .

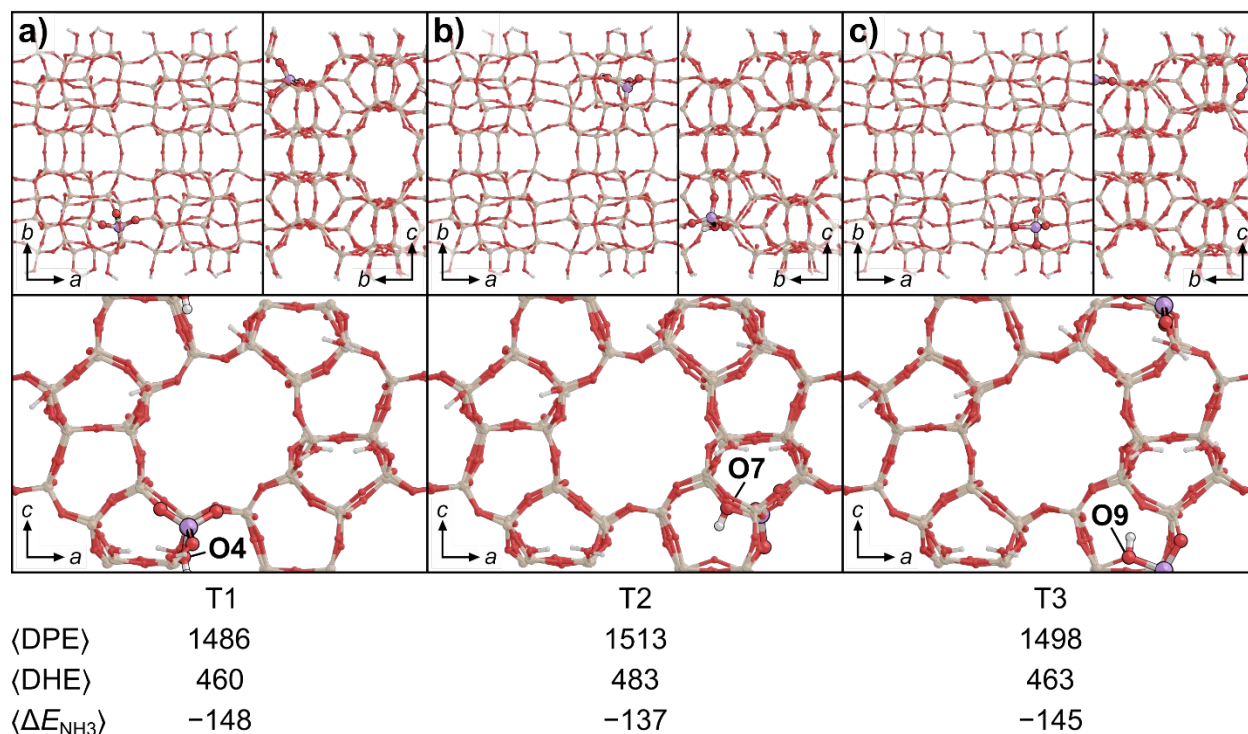


**Figure S12.** Structures of the most stable H-form on the surface model for external Al positions with the proton at (a) O4 on T1, (b) O7 on T2, and (c) O9 on T3. Structures are shown down the  $c$ -vector (top left), down the  $a$ -vector and sinusoidal channel (top right), and down the  $b$ -vector and straight channel (bottom). The ensemble average DPE (extrapolated to 0 Å of vacuum space, see Section 3.2 of the main text), DHE, and  $\Delta E_{\text{NH}_3}$  are shown for each T-site beneath the corresponding structure, all in  $\text{kJ mol}^{-1}$ .

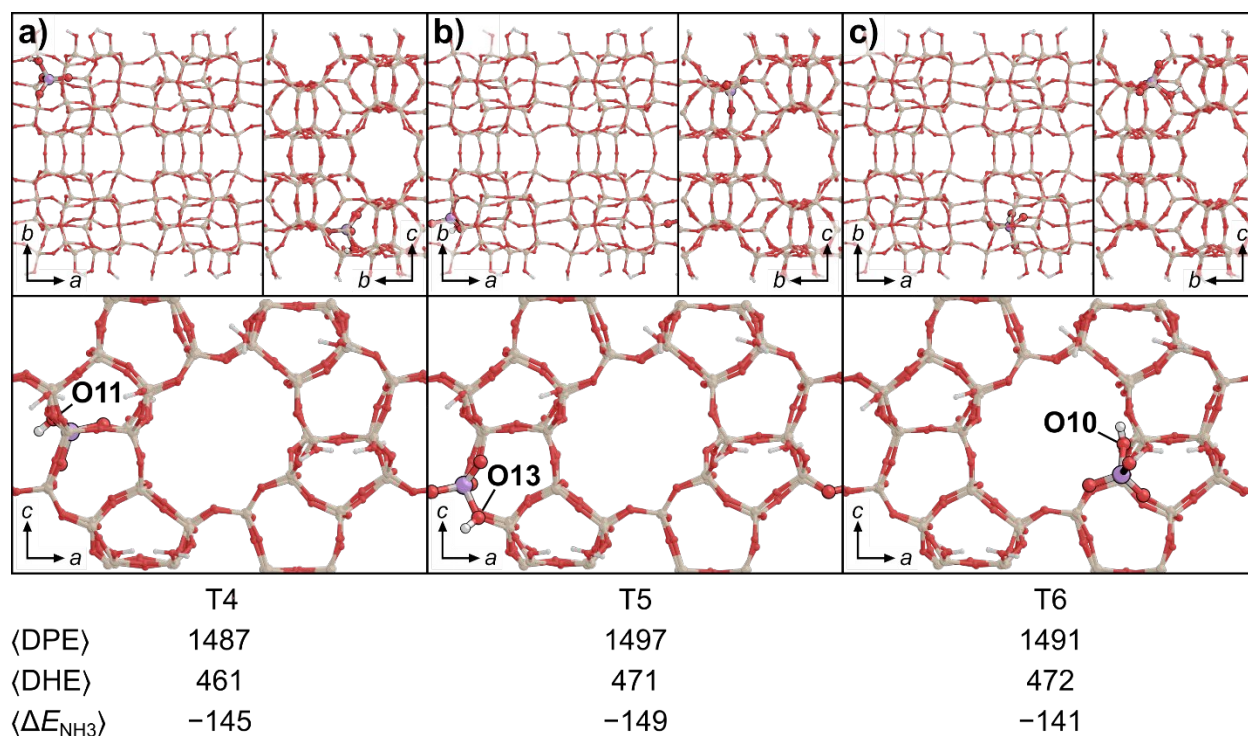


**Figure S13.** Structures of the most stable H-form on the surface model for external Al positions with the proton at (a) O11 on T4, (b) O13 on T5, and (c) O10 on T6. Structures are shown down the  $c$ -vector (top left), down the  $a$ -vector and sinusoidal channel (top right), and down the  $b$ -vector and straight channel (bottom). The ensemble average DPE (extrapolated to 0 Å of vacuum space, see Section 3.2 of the main text), DHE, and  $\Delta E_{\text{NH}_3}$  are shown for each T-site beneath the corresponding structure, all in  $\text{kJ mol}^{-1}$ .



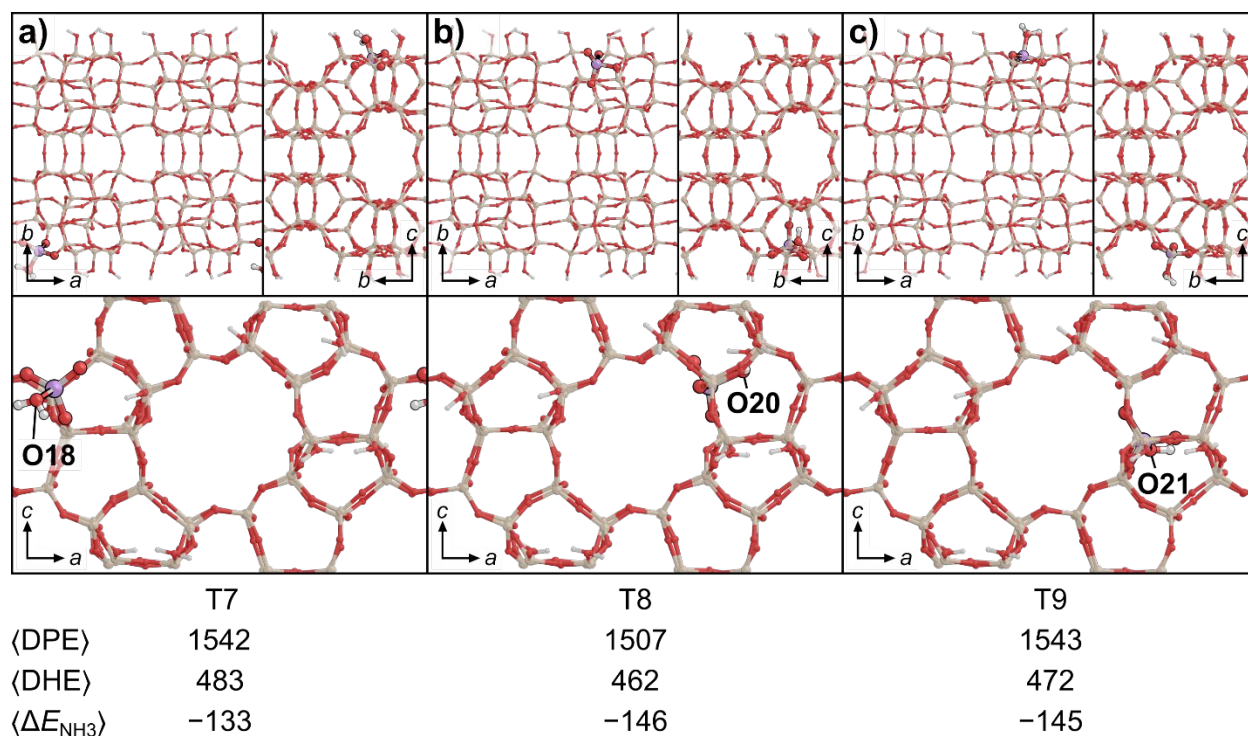


**Figure S14.** Structures of the most stable H-form on the surface model for external Al positions with the proton at (a) O18 on T7, (b) O20 on T8, and (c) O21 on T9. Structures are shown down the  $c$ -vector (top left), down the  $a$ -vector and sinusoidal channel (top right), and down the  $b$ -vector and straight channel (bottom). The ensemble average DPE (extrapolated to 0 Å of vacuum space, see Section 3.2 of the main text), DHE, and  $\Delta E_{\text{NH}_3}$  are shown for each T-site beneath the corresponding structure, all in  $\text{kJ mol}^{-1}$ .

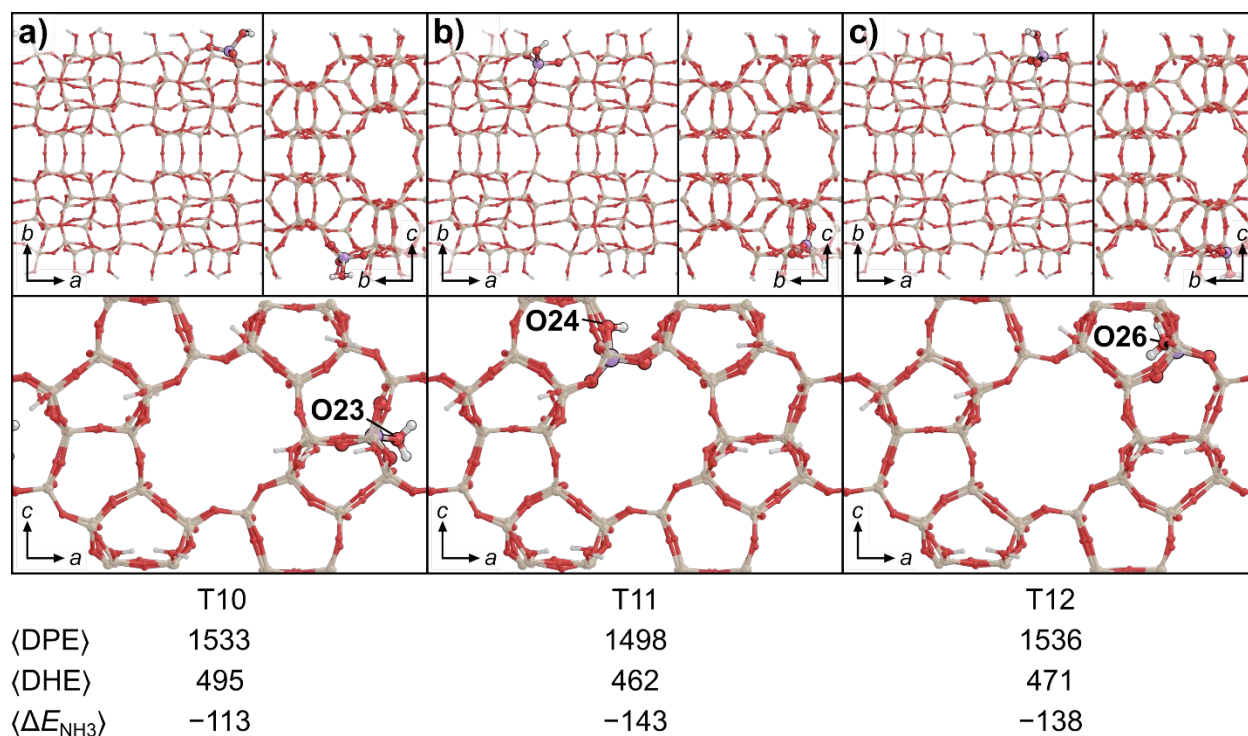


**Figure S15.** Structures of the most stable H-form on the surface model for external Al positions with the proton at (a) O23 on T10, (b) O24 on T11, and (c) O26 on T12. Structures are shown down the  $c$ -vector (top left), down the  $a$ -vector and sinusoidal channel (top right), and down the  $b$ -vector and straight channel (bottom). The ensemble average DPE (extrapolated to 0 Å of vacuum space, see Section 3.2 of the main text), DHE, and  $\Delta E_{\text{NH}_3}$  are shown for each T-site beneath the corresponding structure, all in  $\text{kJ mol}^{-1}$ .

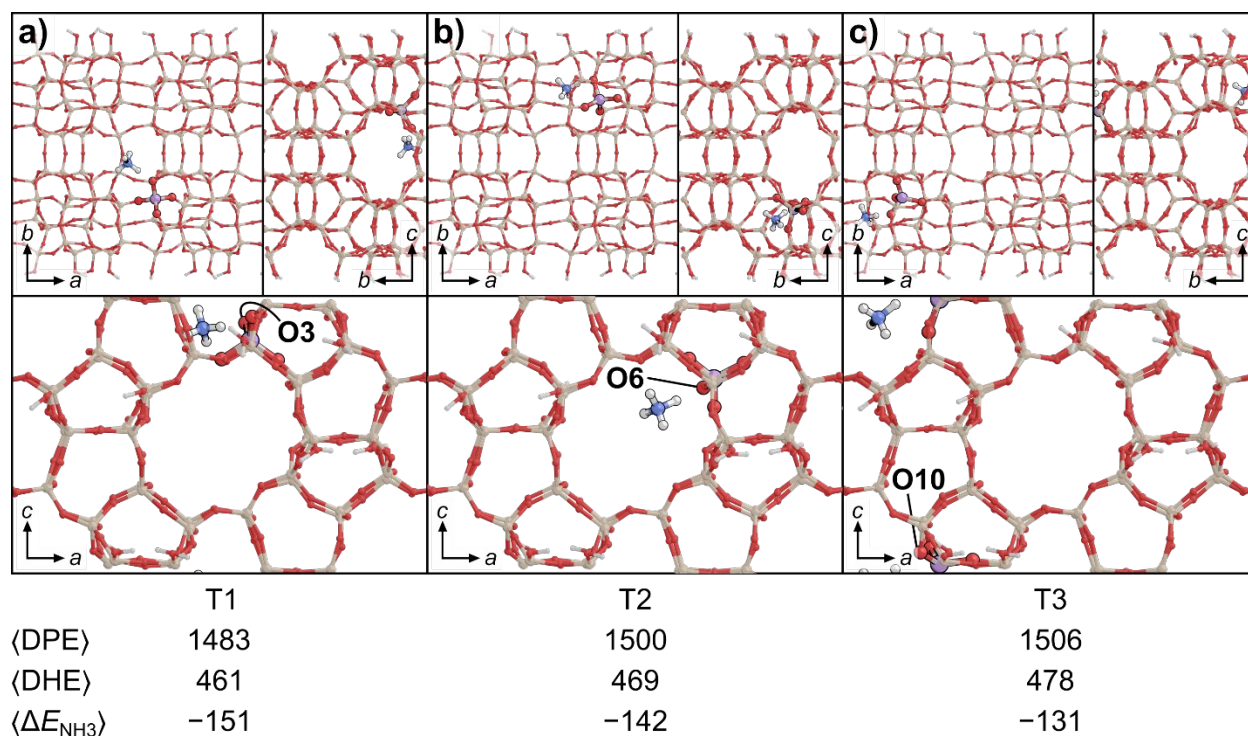


**Figure S16.** Structures of the most stable  $\text{NH}_4$ -form on the surface model for internal Al positions with the  $\text{NH}_4^+$  at (a) O3 on T1, (b) O6 on T2, and (c) O10 on T3. Structures are shown down the  $c$ -vector (top left), down the  $a$ -vector and sinusoidal channel (top right), and down the  $b$ -vector and straight channel (bottom). The ensemble average DPE (extrapolated to 0 Å of vacuum space, see Section 3.2 of the main text), DHE, and  $\Delta E_{\text{NH}_3}$  are shown for each T-site beneath the corresponding structure, all in  $\text{kJ mol}^{-1}$ .



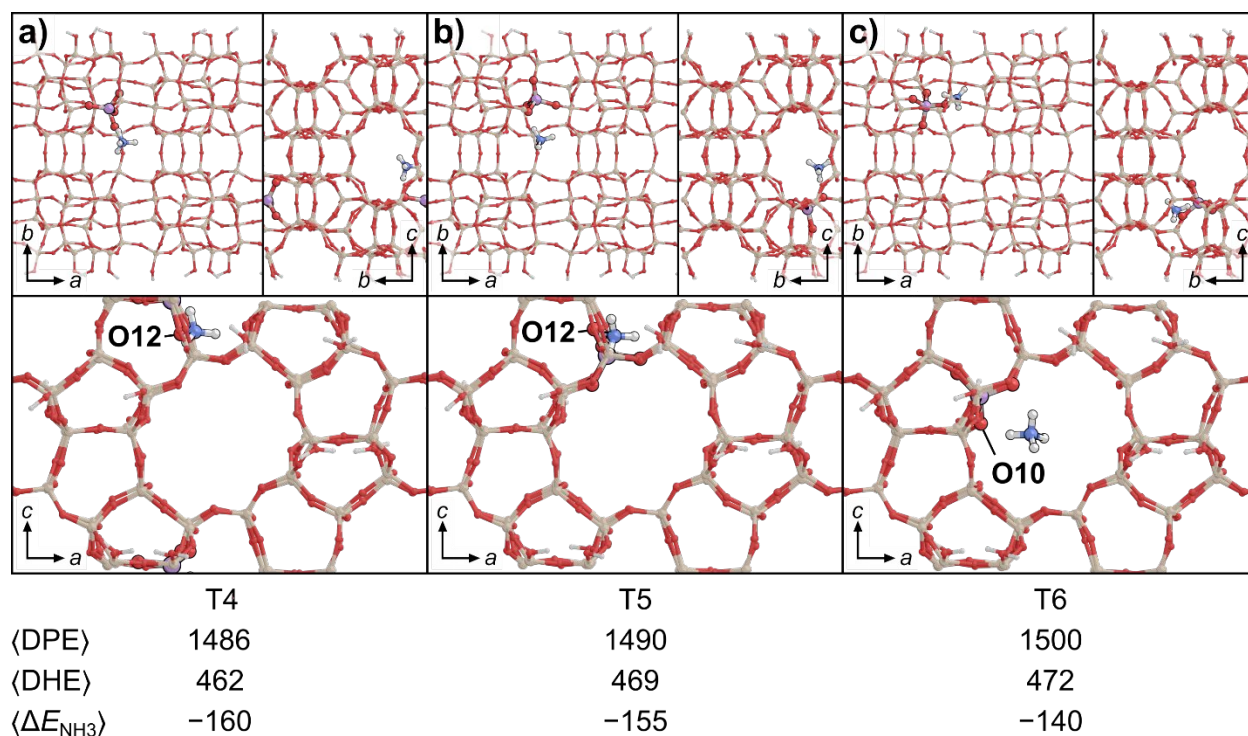


**Figure S17.** Structures of the most stable  $\text{NH}_4$ -form on the surface model for internal Al positions with the  $\text{NH}_4^+$  at (a) O12 on T4, (b) O12 on T5, and (c) O10 on T6. Structures are shown down the  $c$ -vector (top left), down the  $a$ -vector and sinusoidal channel (top right), and down the  $b$ -vector and straight channel (bottom). The ensemble average DPE (extrapolated to 0 Å of vacuum space, see Section 3.2 of the main text), DHE, and  $\Delta E_{\text{NH}_3}$  are shown for each T-site beneath the corresponding structure, all in  $\text{kJ mol}^{-1}$ .

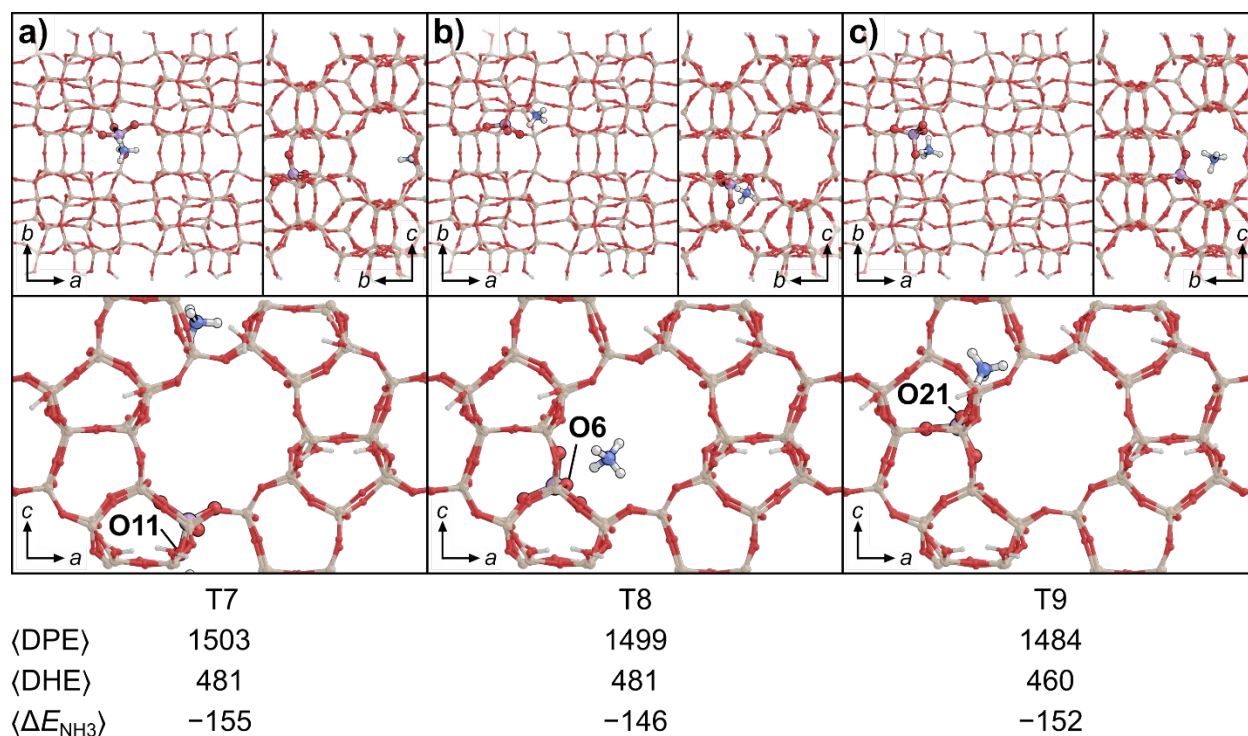


**Figure S18.** Structures of the most stable  $\text{NH}_4^+$  form on the surface model for internal Al positions with the  $\text{NH}_4^+$  at (a) O11 on T7, (b) O6 on T8, and (c) O21 on T9. Structures are shown down the  $c$ -vector (top left), down the  $a$ -vector and sinusoidal channel (top right), and down the  $b$ -vector and straight channel (bottom). The ensemble average DPE (extrapolated to 0 Å of vacuum space, see Section 3.2 of the main text), DHE, and  $\Delta E_{\text{NH}_3}$  are shown for each T-site beneath the corresponding structure, all in  $\text{kJ mol}^{-1}$ .

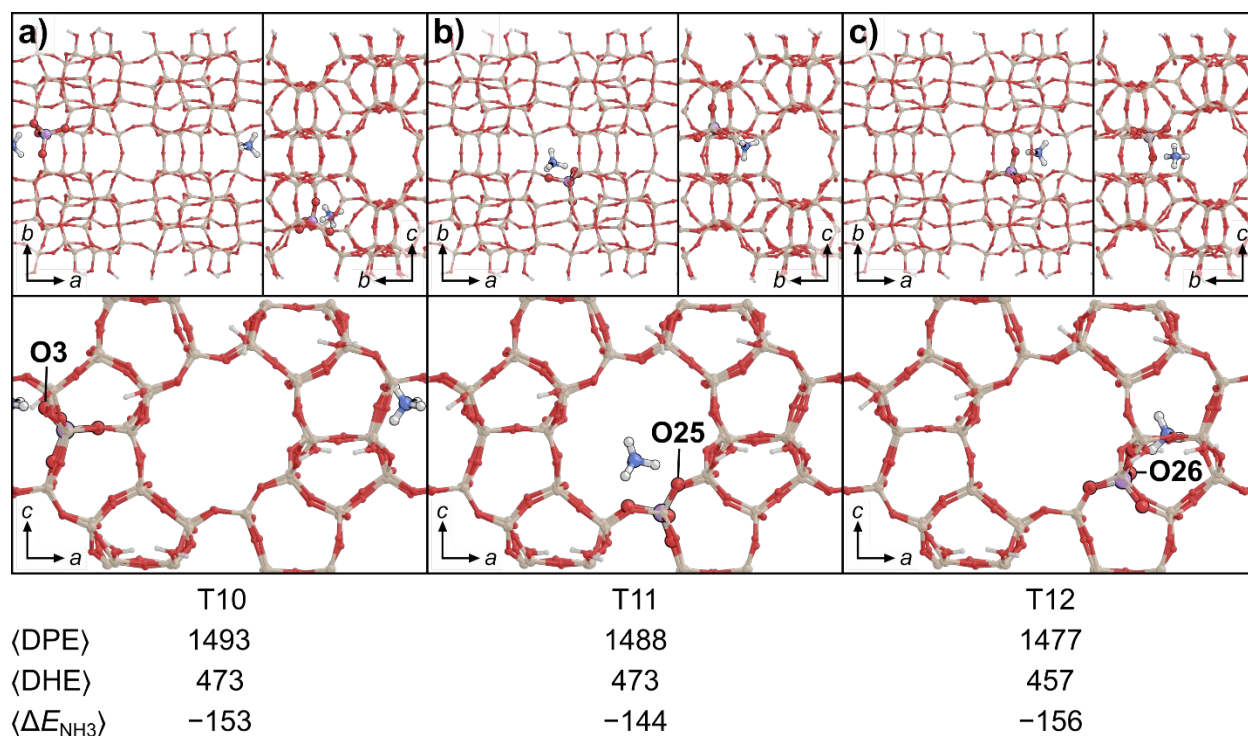


**Figure S19.** Structures of the most stable  $\text{NH}_4^+$ -form on the surface model for internal Al positions with the  $\text{NH}_4^+$  at (a) O3 on T10, (b) O25 on T11, and (c) O26 on T12. Structures are shown down the  $c$ -vector (top left), down the  $a$ -vector and sinusoidal channel (top right), and down the  $b$ -vector and straight channel (bottom). The ensemble average DPE (extrapolated to 0 Å of vacuum space, see Section 3.2 of the main text), DHE, and  $\Delta E_{\text{NH}_3}$  are shown for each T-site beneath the corresponding structure, all in  $\text{kJ mol}^{-1}$ .

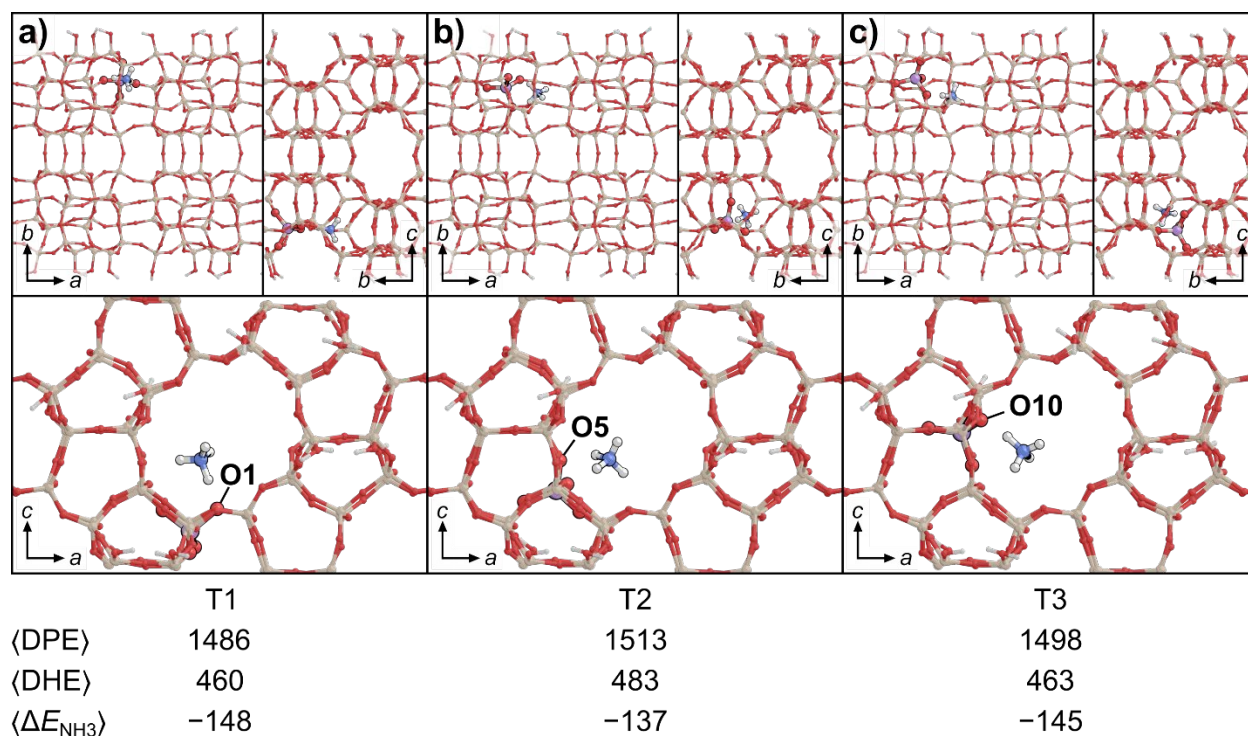


**Figure S20.** Structures of the most stable  $\text{NH}_4^+$  form on the surface model for external Al positions with the  $\text{NH}_4^+$  at (a) O1 on T1, (b) O5 on T2, and (c) O10 on T3. Structures are shown down the  $c$ -vector (top left), down the  $a$ -vector and sinusoidal channel (top right), and down the  $b$ -vector and straight channel (bottom). The ensemble average DPE (extrapolated to 0 Å of vacuum space, see Section 3.2 of the main text), DHE, and  $\Delta E_{\text{NH}_3}$  are shown for each T-site beneath the corresponding structure, all in  $\text{kJ mol}^{-1}$ .

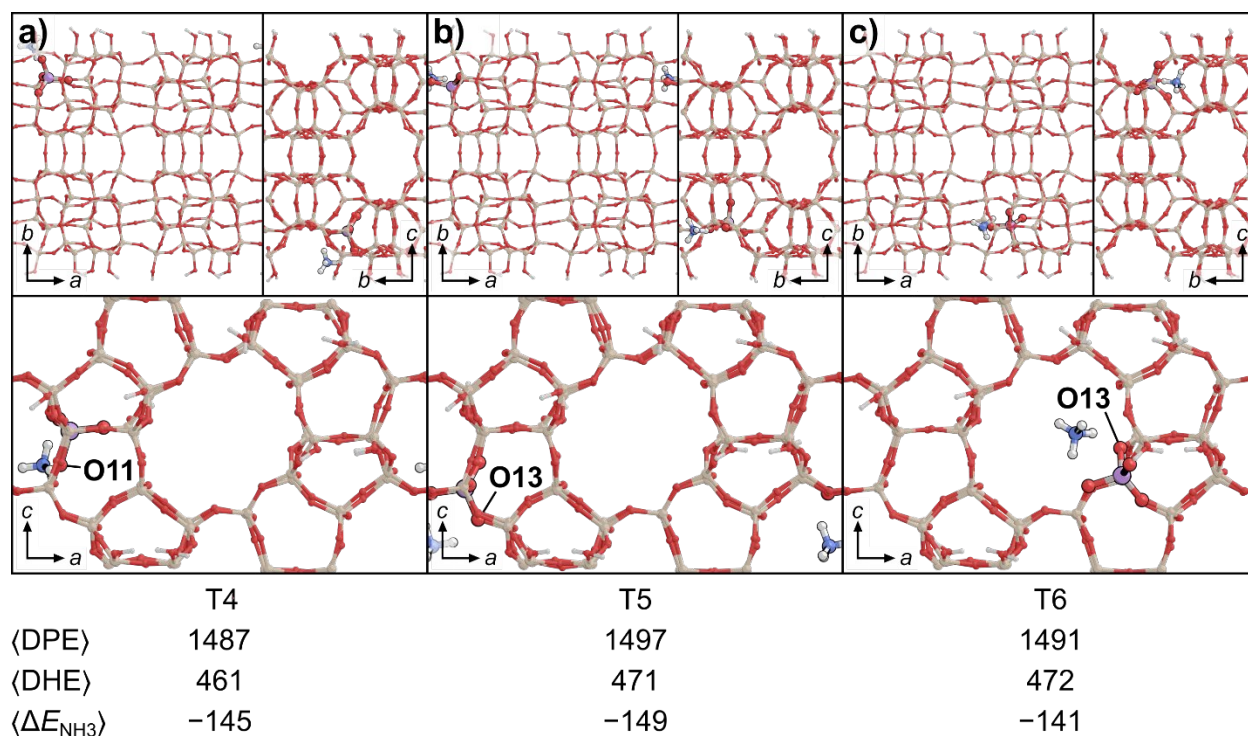


**Figure S21.** Structures of the most stable  $\text{NH}_4$ -form on the surface model for external Al positions with the  $\text{NH}_4^+$  at (a) O11 on T4, (b) O13 on T5, and (c) O13 on T6. Structures are shown down the  $c$ -vector (top left), down the  $a$ -vector and sinusoidal channel (top right), and down the  $b$ -vector and straight channel (bottom). The ensemble average DPE (extrapolated to 0 Å of vacuum space, see Section 3.2 of the main text), DHE, and  $\Delta E_{\text{NH}_3}$  are shown for each T-site beneath the corresponding structure, all in  $\text{kJ mol}^{-1}$ .



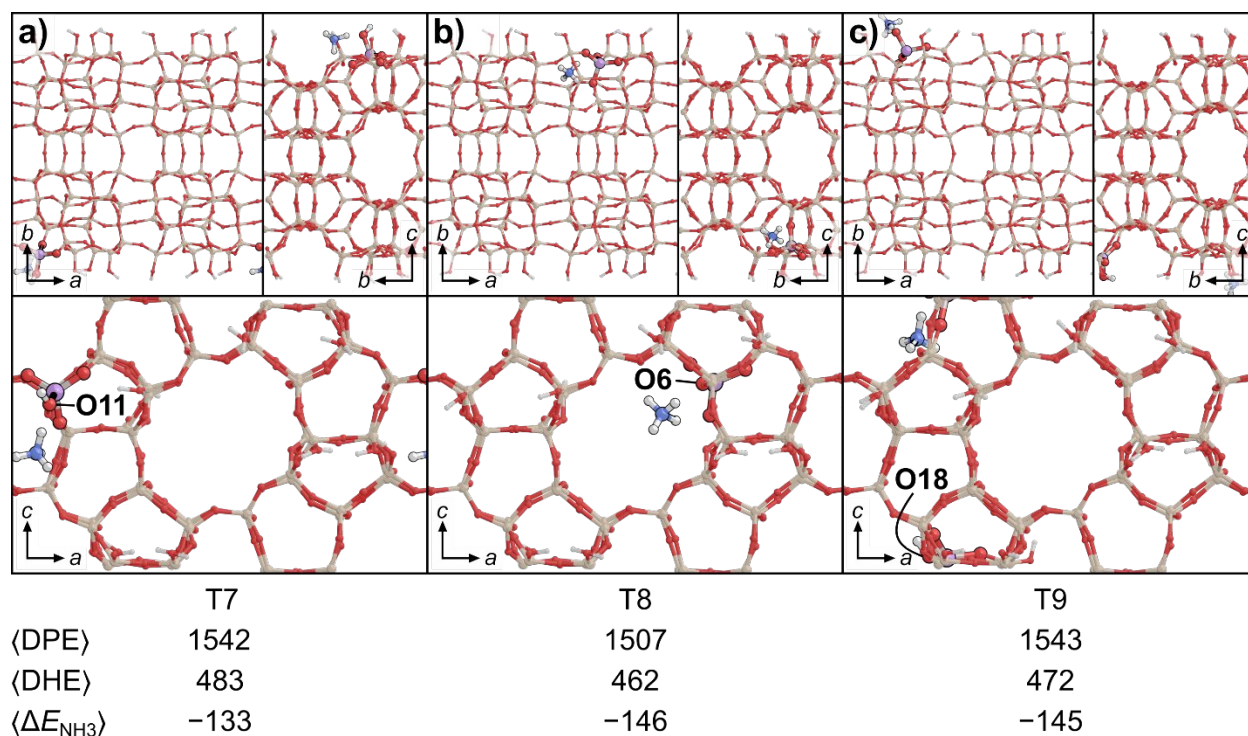


**Figure S22.** Structures of the most stable  $\text{NH}_4^+$  form on the surface model for external Al positions with the  $\text{NH}_4^+$  at (a) O11 on T7, (b) O6 on T8, and (c) O18 on T9. Structures are shown down the  $c$ -vector (top left), down the  $a$ -vector and sinusoidal channel (top right), and down the  $b$ -vector and straight channel (bottom). The ensemble average DPE (extrapolated to 0 Å of vacuum space, see Section 3.2 of the main text), DHE, and  $\Delta E_{\text{NH}_3}$  are shown for each T-site beneath the corresponding structure, all in  $\text{kJ mol}^{-1}$ .

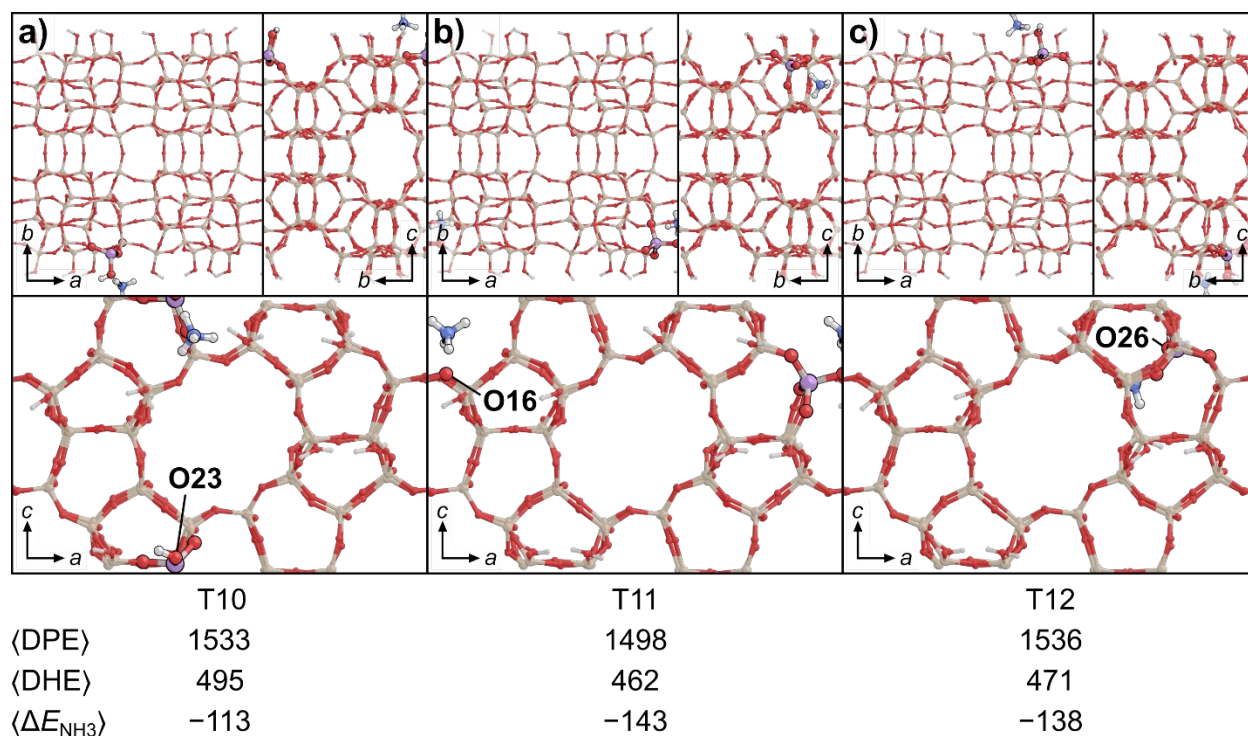


**Figure S23.** Structures of the most stable  $\text{NH}_4$ -form on the surface model for external Al positions with the  $\text{NH}_4^+$  at (a) O23 on T10, (b) O16 on T11, and (c) O26 on T12. Structures are shown down the  $c$ -vector (top left), down the  $a$ -vector and sinusoidal channel (top right), and down the  $b$ -vector and straight channel (bottom). The ensemble average DPE (extrapolated to 0 Å of vacuum space, see Section 3.2 of the main text), DHE, and  $\Delta E_{\text{NH}_3}$  are shown for each T-site beneath the corresponding structure, all in  $\text{kJ mol}^{-1}$ .

## Section S5. DPE dependence on vacuum space in surface model

We varied the vacuum spacing in the MFI surface model and computed DPE at all 12 T-sites to determine how such spacing affects DPE. Calculating DPE requires that the energies of cells with a charge be computed, which is balanced in VASP by a universal compensating background charge that introduces a dipole. As such, varying the vacuum space (and therefore the unit cell size) alters the DPE because charges interact with one another across periodic boundaries. We have noted this interaction in our previous work<sup>1</sup> but also observe similar changes in DPE with unit cell size on this surface MFI model (Figure S24).

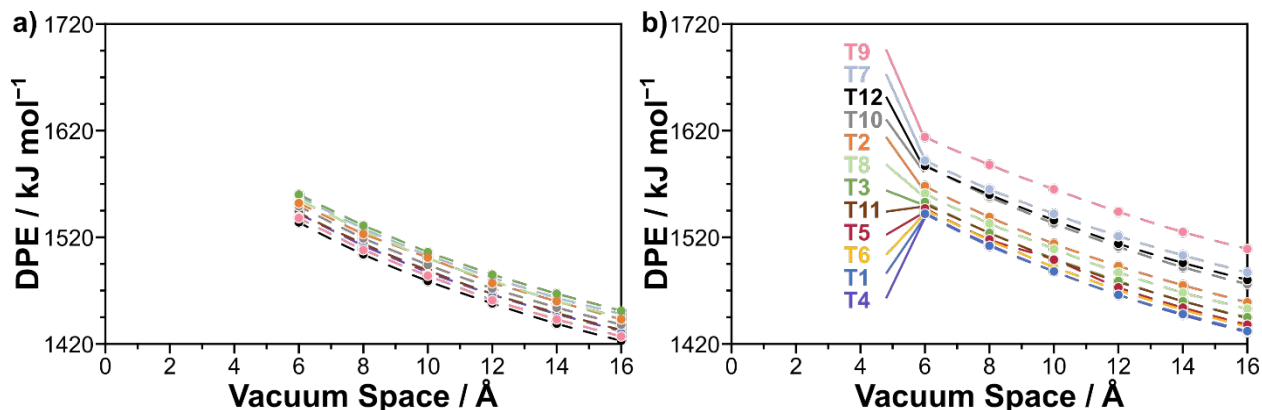


**Figure S24.** DPE for (a) internal and (b) external acid sites as a function of vacuum space added to the MFI surface model used in this work for all 12 T-sites. Dashed lines are to guide the eye.

Initially, we fit a quadratic polynomial to the DPE values in the surface MFI model and used those fits to extrapolate to estimate DPE values with 0  $\text{\AA}$  of vacuum. Ostensibly, this approach would permit us to compare DPE values in the surface model with those of the bulk model with no vacuum added. This formula took the form:

$$DPE = \alpha x^2 + \beta x + \gamma \quad (\text{S1})$$

where  $\alpha$ ,  $\beta$ , and  $\gamma$  were parameters of the fit for each T-site, with  $\gamma$  representing the DPE with 0  $\text{\AA}$  of vacuum space. This approach was not physically meaningful but provided excellent fits ( $r^2 > 0.99$  for all T-sites; Fig. S25). There is no theoretical justification for a quadratic model to fit these data; this fit was applied based on empirical observation alone and because of the goodness of fit (with  $r^2 = 0.99$ –1.00 for the DPE as a function of vacuum space for all models).

While they are more physically meaningful than a simple quadratic fit, Madelung constants<sup>2,3</sup> or Ewald summations<sup>4</sup> cannot be used to model these interactions: neither would converge for this system because there is a net charge and both approaches use infinite sums. Instead, we use a simple fit of Coulomb's law accounting for the two different media through which these interactions occur (a zeolite and vacuum space) improves the physical meaning of extrapolating to 0  $\text{\AA}$  of vacuum space.

We fit a simplified Coulombic potential between two ions across the vacuum space (*i.e.*, only along the  $b$ -vector) that attempts to account for the different media by averaging their contributions



to the permittivity based on the thickness of each slab. Two charges ( $q_1$  and  $q_2$ , both  $-1e$ ) are separated in the  $b$ -direction of the MFI unit cell by the MFI crystal (with thickness  $b_{MFI}$ , the length of the MFI  $b$ -vector) and a variable vacuum layer ( $x$ ) with permittivity values of  $\kappa_{MFI}$  and  $\kappa_0$ , respectively:

$$V = \frac{q_1 q_2}{4\pi \frac{\kappa_{MFI} b_{MFI} + \kappa_0 x}{b_{MFI} + x} (b_{MFI} + x)} = \frac{1}{4\pi (\kappa_{MFI} b_{MFI} + \kappa_0 x)} \quad (S2)$$

In this case, we fit both the  $\kappa_{MFI}$  and  $\kappa_0$  values to the ensemble average DPE data for each T-site location and extrapolate to 0 Å vacuum space. Generally, the Coulombic model predicts higher DPE values than the quadratic model with 0 Å of vacuum space on the surface MFI model (Figure S25). Notably, both the quadratic and Coulombic fits provide excellent fits to the data, with  $r^2 = 1.00$  for T1 (with similar  $r^2$  values and constants for other T-sites); however, these models have significantly different limiting behavior (Figure S26). Coulombic interactions that govern the stability of the deprotonated form of the zeolite indicate that DPE estimates should decay as vacuum spacing increases (because the anion becomes more stable) and eventually reach their asymptotic value. This is true for both the Coulombic model, but not for the quadratic model (Fig. S26).

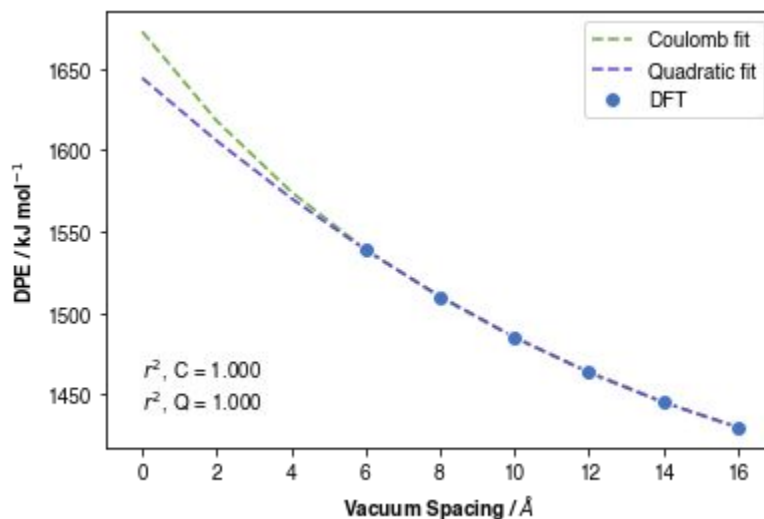


**Figure S25.** DPE values at the internal T1 site of the MFI surface model (blue circles) with fitted models for a multi-permittivity Coulombic fit (green line) and a quadratic fit (purple). Goodness-of-fit parameters ( $r^2$ ) for the Coulombic (C) and quadratic (Q) models are shown in the bottom right of the plot.

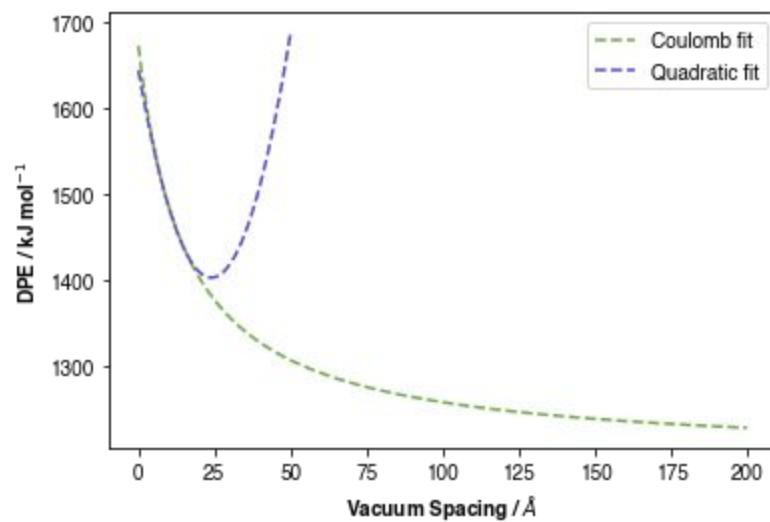


**Figure S26.** Limiting behavior of the Coulombic (green) and quadratic (purple) models on the internal T1 Al location of the surface MFI model as a function of vacuum thickness.

## Section S6. Derivation of rate ratio equation for external and internal sites

The relative ratio of the rates at external and internal sites Brønsted acid sites in zeolites ( $H^+$ ) depends on:

- the densities of protons inside and outside the zeolite (related to the Si/Al ratio)
- the confinement of reactive intermediates within and without the zeolite (which affects the  $k$  values)
- the surface area ( $A_s$ ) to volume ( $V$ ) ratio of particles in the reactor ( $A_s/V$ )
- the Thiele modulus ( $\Phi$ ) and the effectiveness factor ( $\eta$ )
- the size and shape of the catalyst particles (which affect  $A_s/V$ ,  $\Phi$ , and  $\eta$ )

The effectiveness factor,  $\eta$ , is a function of the Thiele modulus, which is in turn a function of several other values:

$$\eta = f(\Phi^2) = f(k_{int}, \mathcal{D}_{eff}, T, L) \quad (S2)$$

where  $k_{int}$  is the rate constant at internal sites,  $L$  is a characteristic length,  $\mathcal{D}_{eff}$  is the effective diffusivity, and  $T$  is the temperature.

The formulas for  $\eta$  and for  $\Phi$  change depending on the shape of the particle. The Thiele modulus is generally described by:

$$\Phi = \frac{L}{\alpha} \sqrt{\frac{k_{int} C_{A,surf}^{n-1}}{\mathcal{D}_{eff}}} \quad (S3)$$

where  $n$  is the reaction order,  $L$  is a characteristic length—the radius of a sphere or cylinder (typically represented with  $R$ ) or half the thickness of a slab (typically represented by  $L$ )— $C_{A,surf}$  is the concentration of the reactant at the surface, and  $\alpha$  is a shape parameter, which can be 3 for a sphere, 2 for a cylinder, or 1 for a slab. If we assume that there are no mass transport limitations between the bulk and the surface and that conversion remains extremely low, then  $C_{A,surf}$  is just the inlet concentration.

The effectiveness factor depends on the Thiele modulus, but the relationship between them depends on the shape of the particle. The most commonly employed equations for effectiveness factor are those for spherical and slab-shaped particles:

$$\eta_{sphere} = \frac{3}{\Phi^2} (\Phi \coth \Phi - 1) \quad (S4)$$

$$\eta_{slab} = \frac{\tanh \Phi}{\Phi} \quad (S5)$$

The ratio of the net rate on external and internal sites can be represented by the equation

$$\frac{r_{ext}}{r_{int}} = \frac{\left( \frac{r''_{ext}}{[H^+]_{ext}} \right) \left( \frac{[H^+]_{ext}}{A_s} \right) A_s}{\left( \frac{r''_{int}}{[H^+]_{int}} \right) \left( \frac{[H^+]_{int}}{V} \right) V} = \frac{k_{ext} C_{A,surf} \rho_{H^+,ext} A_s}{\eta k_{int} C_{A,surf} \rho_{H^+,int} V} \quad (S6)$$

where  $\rho_{H^+}$  is the density of protons on the surface or in the bulk. These densities are determined by the Si/Al ratio on the surface and in the bulk of the zeolite and the fraction of Al sites that form only Brønsted acid sites,  $Al_B/Al_{tot}$  (*i.e.*, are not substituted at silanol (SiOH) positions to form Lewis acid sites):

$$\rho_{H^+,int} = \frac{[H^+]_{int}}{V} = \rho_{T,int} \left( \frac{Si}{Al} \right)_{int}^{-1} \quad (S7)$$

$$\rho_{H^+,ext} = \frac{[H^+]_{ext}}{A_s} = \rho_{T,ext} \left( \frac{Si}{Al} \right)_{ext}^{-1} \left( \frac{Al_B}{Al_{tot}} \right) \quad (S8)$$

where  $\rho_{T,ext}$  and  $\rho_{T,int}$  are the spatial densities of T-sites on the surface ( $\text{\AA}^{-2}$ ) and in the bulk ( $\text{\AA}^{-3}$ ). For the MFI model employed in this work, these values are  $0.0894 \text{ \AA}^{-2}$  and  $0.0180 \text{ \AA}^{-3}$ , respectively. These equations assume that the proportion of extraframework Al is insignificant and that the Si/Al ratio is a sufficient representation for the density of Brønsted acid sites in the bulk and on the surface (when accounting for the number of possible Lewis acid substitution locations in the latter case). Substituting equations S7 and S8 into equation S6 yields

$$\frac{r_{ext}}{r_{int}} = \frac{k_{ext}\rho_{H^+,ext}A_s}{\eta k_{int}\rho_{H^+,int}V} = \left( \frac{k_{ext}}{k_{int}} \right) \left( \frac{\rho_{T,ext}}{\rho_{T,int}} \right) \left( \frac{\left( \frac{Si}{Al} \right)_{ext}^{-1} \left( \frac{Al_B}{Al_{tot}} \right)}{\left( \frac{Si}{Al} \right)_{int}^{-1}} \right) \left( \frac{A_s}{V} \right) \eta^{-1} \quad (S9)$$

Moreover, if the Si/Al ratios within and at the surface of these materials is the same, then the equation simplifies further to

$$\frac{r_{ext}}{r_{int}} = \left( \frac{k_{ext}}{k_{int}} \right) \left( \frac{\rho_{T,ext}}{\rho_{T,int}} \right) \left( \frac{Al_B}{Al_{tot}} \right) \left( \frac{A_s}{V} \right) \eta^{-1} \quad (S10)$$

The equations for  $\eta$  as functions of  $\Phi$  for different catalyst models can then be substituted into this model to estimate the effects of particle size on the relative contribution of external and internal sites for a given reaction. Additionally, the value of  $A_s/V$  depends only on the characteristic length of the model being employed. For a sphere with radius  $R$ ,

$$\left( \frac{A_s}{V} \right)_{sphere} = \frac{4\pi R^2}{\frac{4}{3}\pi R^3} = \frac{3}{R} \quad (S11)$$

For a slab of thickness  $2L$  (which is the only direction in which diffusion occurs) and with height  $a$  and width  $b$  (where no diffusion occurs), the relevant value of  $A_s/V$  is

$$\left( \frac{A_s}{V} \right)_{slab} = \frac{ab}{2Lab} = \frac{1}{2L} \quad (S12)$$

The  $A_s/V$  can be estimated from the fraction of Brønsted sites that are on the outside of the catalyst ( $f_{ext}$ ), assuming that  $\rho_{T,ext}$ ,  $\rho_{T,int}$ , and  $Al_B/Al_{tot}$  values remain constant or similar for different MFI facets. This fraction is represented by

$$f_{ext} = \frac{\text{number of external } H^+}{\text{number of total } H^+} = \frac{\left( \frac{Si}{Al} \right)_{ext}^{-1} \left( \frac{Al_B}{Al_{tot}} \right) \rho_{T,ext} A_s}{\left( \frac{Si}{Al} \right)_{int}^{-1} \rho_{T,int} V + \left( \frac{Si}{Al} \right)_{ext}^{-1} \left( \frac{Al_B}{Al_{tot}} \right) \rho_{T,ext} A_s} \quad (S13)$$

If the Si/Al ratio is constant within and on the outside of the zeolite particle, then the  $A_s/V$  is

$$\frac{A_s}{V} = \frac{f_{ext}\rho_{T,int}}{(1 - f_{ext})\left(\frac{Al_B}{Al_{tot}}\right)\rho_{T,ext}} \quad (S14)$$

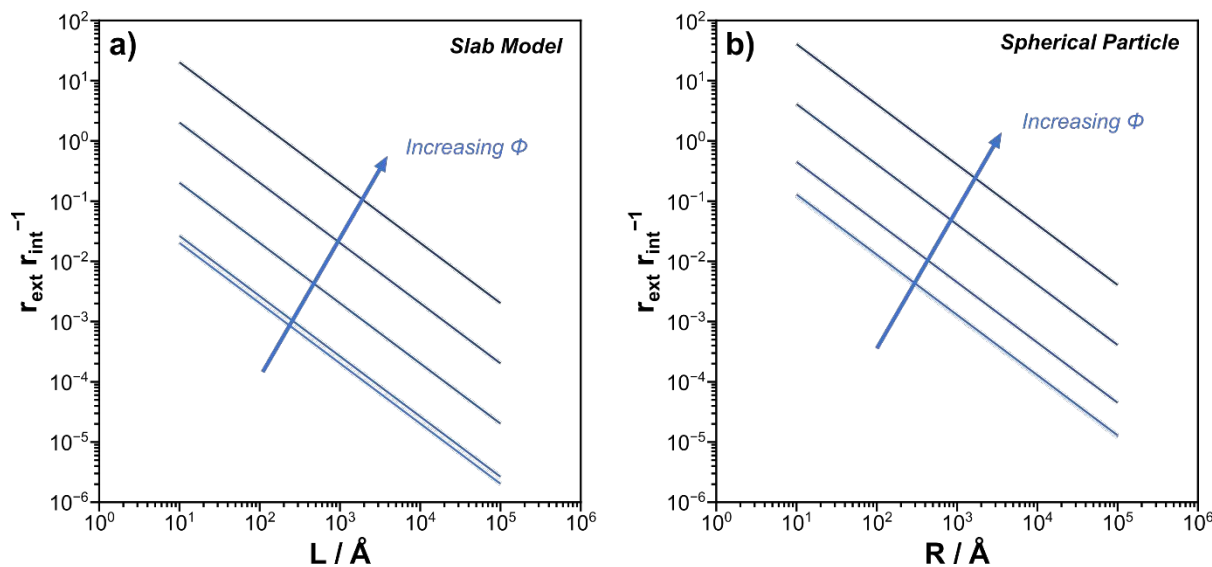


**Figure S27.** Ratio of rates on external sites to those on internal sites ( $r_{ext}/r_{int}$ ) as a function of the characteristic length in (a) a slab model (half the thickness,  $L$ ) and (b) a spherical particle model (radius of the sphere,  $R$ ). Rate ratios are shown for Thiele moduli ( $\Phi$ ) of  $10^{-1}$ ,  $10^0$ ,  $10^1$ ,  $10^2$ , and  $10^3$ .

## References

- (1) Nystrom, S.; Hoffman, A.; Hibbitts, D. Tuning Brønsted acid strength by altering site proximity in CHA framework zeolites. *ACS Catal.* **2018**, 8, 7842–7860.
- (2) Kittel, C. *Introduction to Solid State Physics*; 7th ed.; Wiley: New York, 1995; p. 688.
- (3) Madelung, E. Das elektrische Feld in Systemen von regelmäßig angeordneten Punktladungen. *Phys. Z* **1918**, 19.
- (4) Ewald, P. P. Die Berechnung optischer und elektrostatischer Gitterpotentiale. *Ann. Phys.* **1921**, 369, 253–287.